On the Use of Black Ti as a Bone Substituting Biomaterial

Behind the Scenes of Dual-Functionality

Modaresifar, Khashayar; Ganjian, Mahya; Angeloni, Livia; Minneboo, Michelle; Ghatkesar, Murali K.; Hagedoorn, Peter Leon; Fratila-Apachitei, Lidy E.; Zadpoor, Amir A.

DOI
10.1002/smll.202100706

Publication date
2021

Document Version
Final published version

Published in
Small

NANO · MICRO small
www.small-journal.com

On the Use of Black Ti as a Bone Substituting Biomaterial: Behind the Scenes of Dual-Functionality

Khashayar Modaresifar, Mahya Ganjian, Livia Angeloni, Michelle Minneboo, Murali K. Ghatkesar, Peter-Leon Hagedoorn, Lidy E. Fratila-Apachitei, and Amir A. Zadpoor*

Despite the potential of small-scale pillars of black titanium (bTi) for killing the bacteria and directing the fate of stem cells, not much is known about the effects of the pillars' design parameters on their biological properties. Here, three distinct bTi surfaces are designed and fabricated through dry etching of the titanium, each featuring different pillar designs. The interactions of the surfaces with MC3T3-E1 preosteoblast cells and *Staphylococcus aureus* bacteria are then investigated. Pillars with different heights and spatial organizations differently influence the morphological characteristics of the cells, including their spreading area, aspect ratio, nucleus area, and cytoskeletal organization. The preferential formation of focal adhesions (FAs) and their size variations also depend on the type of topography. When the pillars are neither fully separated nor extremely tall, the colocalization of actin fibers and FAs as well as an enhanced matrix mineralization are observed. However, the killing efficiency of these pillars against the bacteria is not as high as that of fully separated and tall pillars. This study provides a new perspective on the dual-functionality of bTi surfaces and elucidates how the surface design and fabrication parameters can be used to achieve a surface topography with balanced bactericidal and osteogenic properties.

1. Introduction

The increased life expectancy of humankind has encouraged the medical device industry to develop functional devices that outlive the patients. In this regard, bone implants require a long list of properties and functionalities to serve their purpose most properly. In addition to primary stability[1,2] and bone-matching mechanical properties,[3] bone implants need to be designed in such a way to promote host tissue regeneration and integration with the implant (i.e., osteoinduction and osseointegration),[4–6] as well as to combat implant-associated infections (IAIs),[7–9] as one of the main causes of implant failure.

Developing designer biomaterials with better control over their biological properties and interactions with their host is proven crucial for enhancing the performance of implantable medical devices.[10] Yet achieving the optimal biological properties and controlling the interactions of bio-organisms with the biomaterial are highly dependent on the surface properties.[11–14] For instance, enhancing cell adhesion, cell growth,[15,16] and the desired differentiation of stem cells[17,18] are among the steps required to optimize the osseointegration of implants. Similarly, preventing IAIs through the eradication of the adherent bacteria and the aversion of biofilm formation play important roles in this regard.[19] To this aim, exploiting the advances in surface modification techniques is a necessity to achieve those rare or unprecedented properties as the surface is the frontline where the success of a biomaterial is determined. Due to the complications associated with the use of antibacterial agents[20,21] and growth factors,[22] including the high cost and resistance development by bacterial strains, the focus has largely shifted to the physical alterations of the surface.

Given the fact that the physical small-scale features of the surface play a vital role both in directing stem cells fate and resisting the bacterial colonization,[11] the optimization of these features in terms of shape and geometry, dimensions, and spatial arrangement is of high importance.[23,24] The adhesion of mammalian cells to the surface is facilitated via their transmembrane proteins, including integrins that act mechanically to bind the cell to its extracellular matrix (ECM).[25] The formation of focal adhesions (FAs) links the cell cytoskeleton to these integrin clusters and functions as a bridge for transferring physicomechanical stimuli (e.g., mechanical forces) from ECM to the nuclei. These complex and dynamic processes result in different interpretations of various surface topographies by the cells and may upregulate the expression of specific proteins

K. Modaresifar, M. Ganjian, Dr. L. Angeloni, M. Minneboo, Dr. L. E. Fratila-Apachitei, Prof. A. A. Zadpoor
Department of Biomechanical Engineering
Faculty of Mechanical, Maritime, and Materials Engineering
Delft University of Technology
Mekelweg 2, Delft 2628 CD, The Netherlands
E-mail: k.modaresifar@tudelft.nl

Dr. L. Angeloni, Dr. M. K. Ghatkesar
Department of Precision and Microsystems Engineering
Faculty of Mechanical, Maritime, and Materials Engineering
Delft University of Technology (TU Delft)
Mekelweg 2, Delft 2628 CD, The Netherlands

Dr. P.-L. Hagedoorn
Department of Biotechnology
Faculty of Applied Sciences
Delft University of Technology
Van der Maasweg 9, Delft 2629 HZ, The Netherlands

The ORCID identification number(s) for the author(s) of this article can be found under https://doi.org/10.1002/smll.202100706.

DOI: 10.1002/smll.202100706

in certain cell lines.[26,27] Therefore, even subtle variations in the roughness,[28] geometry,[29] and dimensions of the physical features of the implant surface[30,31] may substantially impact the cell behavior. The recent advancements in nano-/microfabrication techniques have facilitated the fabrication of precisely controlled surface topographies, also known as surface patterns,[29] which are capable of inducing osteogenic differentiation in stem cells.[32–34] The effects of different length scales on the osteogenic properties of the patterns is, however, not yet fully comprehended as contradictory effects have been reported for the different relevant length scales in the literature.[33,35,36] Furthermore, one cannot easily correlate the short-term effects of patterns on cell morphology, spreading area, expression of FAs, and cytoskeleton organization with their long-term effects on the expression of osteogenic markers and matrix mineralization. Despite the vast efforts in the recent years, the list of unknowns remains long because there are a plethora of design parameters (e.g., geometry and arrangement), each imposing their influence on cells besides the complexity of cell structure and its intracellular pathways, which are not thoroughly understood till now.[23,37]

On the other hand, inspired by the unique naturally occurring structures,[38–40] synthetic bactericidal surface patterns have emerged with different geometries and dimensions.[41] Patterns that lie within a specific range of dimensions have been shown to mechanically kill different types of bacteria through a combination of different mechanisms.[24,42,43]

Among numerous nano-/microfabrication techniques, reactive ion etching (RIE) is a simple and fast technique for creating an engineered surface topography.[44] RIE works based on dry chemical etching and physical ion bombardment of the surface. Ivanova et al. used RIE to create high aspect ratio nanopillars on a silicon substrate and studied their bactericidal properties for the first time.[45] The killing efficiency of the so-called black silicon (bSi, due to its black appearance) against both Gram-negative and Gram-positive bacteria was comparable to naturally occurring bactericidal surfaces. Ever since, many studies have investigated the effects of the height and density of nanopillars on the bactericidal properties of bSi, as well as the involved killing mechanisms.[46,47] Later on, Hasan et al. successfully fabricated similar nanopillars on a titanium substrate (a more relevant choice of material for orthopedic applications) using inductively coupled plasma RIE (ICP RIE).[48] They showed that bTi is as effective as bSi in killing the bacteria. Moreover, not only did bTi support the attachment and proliferation of human mesenchymal stem cells (hMSCs) but also displayed a synergistic effect in stimulating the osteogenic differentiation of cells together with the osteogenic culture medium. So far, all the mentioned studies have produced bSi and bTi under identical conditions and have only changed the etching time as a variable to achieve different pillar lengths, whereas the geometry and organization of the pillars have been quite comparable in those studies. Recently, the effects of all the processing parameters of ICP RIE on the physicomechanical characteristics of the resulting bTi nanostructures have been systematically studied.[44] Changing other processing parameters, such as the chamber pressure and temperature can also be used to fabricate distinct nanostructured surfaces.

Due to the remarkable structural and biological differences between mammalian and bacterial cells, designing a patterned surface that fulfills dual functionality is quite challenging. In this regard, bTi seems to be a very promising biomaterial for future clinical applications, given that it holds the potential for narrowing down the gap between osteogenic and bactericidal patterns as the essential step in developing cell-instructive biomaterials. However, there are still many unknowns about the behavior of cells interacting with bTi nanopillars and how their long-term osteogenic response is related to their short-term responses (e.g., morphology, spreading area, the formation of FAs, etc.).

In the present study, we provide a new perspective on the dual-functionality of different bTi surfaces with the ultimate aim of devising a guideline for the application of bTi. We hypothesized that the viability and fate of bacteria and mammalian cells are significantly affected by the processing parameters of bTi surfaces and the geometrical characteristics of the pillars covering them. By adjusting the various ICP RIE processing parameters, we produced different types of bTi surfaces in our preliminary studies and selected three out of those that represent a gradual deviation from the flat Ti surface. These three types of bTi are distinct in terms of the height and spatial organization of their pillars. To answer the research question, cytocompatibility, morphological characteristics, the formation of FAs, and the osteogenic response of MC3T3-E1 preosteoblast cells cultured on these three different bTi surfaces, were quantitatively analyzed and the relationships between them were discussed. Furthermore, the bactericidal properties of the same bTi surfaces against *Staphylococcus aureus* bacteria (as the main relevant infectious pathogen involved in IAIs) were evaluated to enable the possible identification of a bTi surface with the desired dual-functionality and to shed light on the possible killing mechanism of the studied surfaces.

2. Results

2.1. Physicochemical Characterization of bTi Surfaces

All Ti surfaces appeared black after the completion of the etching process as expected, due to the light absorption within the fabricated structures.[45,48] Scanning electron microscopy (SEM) observations showed that three types of surface topography had been created on Ti (**Figure 1**A). These were distinguishable based on their geometry and spatial organization, by changing two processing parameters, namely chamber pressure and temperature. The Ti surface topography changed from the polished flat surface (Figure S1A, Supporting Information) due to the formation of pillar-shaped structures on the surface. A temperature of 0 °C and a chamber pressure of 4.0 Pa resulted in closely-packed and short pillars, mainly connected to each other at the tip, hence resembling a porous-like surface when viewed from the top. This type of bTi is, therefore, referred to as Porous. Here, the grain boundaries of the original polished surface were also visible (Figure 1A). By increasing the temperature to 40 °C and decreasing the pressure to 2.0 Pa, the pillars appeared to be taller and more separated from each other, meaning that the height of the pillars became distinguishable

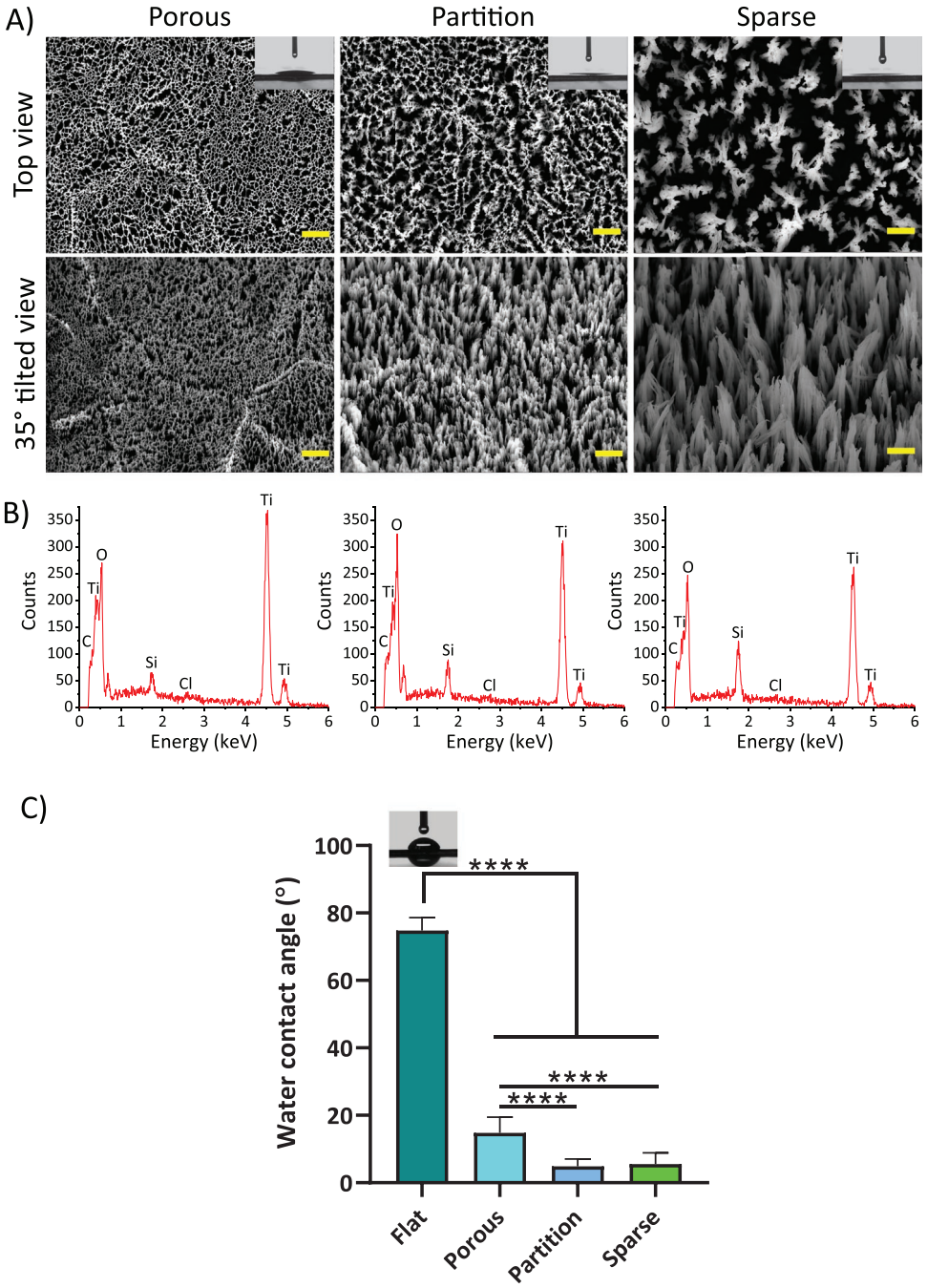

Figure 1. A) The top- and tilted-view SEM images of the Porous, Partition, and Sparse bTi specimens made through ICP RIE, showing distinct surface morphologies and spatial organization of the pillars. The insets depict the water droplets residing on each surface after 5 s. Scale bar = 1 µm. B) Representative EDS spectra of Porous, Partition, and Sparse bTi specimens, showing the most abundant chemical elements identified on each surface. C) The mean water contact angle of the bTi surfaces as compared to the flat Ti surface. ****$p < 0.0001$.

to some extent in the SEM images. The pillars were, however, still connected to some degree, forming partitions of pillars on the surface. Keeping the temperature at 40 °C while decreasing the pressure to 0.5 Pa resulted in the third type of morphology in which the pillars were taller and relatively highly separated from each other, meaning that the height of the pillars could be measured. These pillars also showed clustering at the tip creating free interspaces between the clusters (Figure 1A). Henceforward, we call the former type of bTi Partition and the latter Sparse. Unlike controlled patterns consisting of surface pillars,[24] it is not easy to attribute a precise interspacing value to these surface features. Precise, objective measurement of the diameter of the single pillars was also difficult as many pillars were closely connected to each other, especially in the Porous and Partition samples. However, the tip diameter of the pillars was always <100 nm. From the SEM images it could

be estimated that the height of the pillars increased from the submicron scale, from ≈350 nm in the Porous, to a range of 700 nm to 1 μm in Partition, and then to the microscale in the Sparse samples (a range of 1.4 to 2.2 μm) (Figure 1A). Further atomic force microscopy (AFM) characterizations revealed that due to the formation of the pillars, the average roughness (R_a) of the surfaces increased from <50 nm in the Porous group to >150 nm in the Partition and Sparse groups (Table S1, Supporting Information). Furthermore, the chemical characterization of the bTi surfaces indicated that the most abundant chemical elements of the surface are Ti and O (Figure 1B).

Additionally, while the flat Ti surface showed a static water contact angle of ≈75°, the bTi surfaces exhibited significantly lower contact angles, indicating their superhydrophilic properties. The approximate water contact angle measured for the Porous surface was 15°, which significantly decreased to <6.0° for the Partition and Sparse groups (Figure 1C).

2.2. Short-Term Response of Preosteoblast Cells

MC3T3-E1 preosteoblast cells showed different morphologies on the different types of bTi after 1 day in culture (**Figure 2**A). While the cells possessed a well-spread and polygonal shape on flat Ti, their directionality highly increased on the etched samples, from the Porous to the Partition and to the Sparse specimens (Figure 2A). This change in shape was associated with a decrease in cell area and an increase in the aspect ratio (Figure 2A and **Figure 3**A,B). On the Partition samples, the cells developed long filopodia around cell periphery to attach on these surfaces whereas on the Sparse surfaces, the majority of the cells were highly elongated with a significant number of the cells also showing to be isotropic (i.e., nearly fully rounded). None of the bTi surfaces were found to be cytotoxic, as the results of the PrestoBlue assay showed that the metabolic activity of the cells significantly increased over the course of the 14 days of culture without any significant differences compared to the flat Ti (Figure 2B). Moreover, the cells did not show any profound preferential adhesion toward any of the surfaces (flat Ti and bTi) as the average number of the adhered cells per mm^2 of the specimen surface was not significantly different between any of the experimental groups, including the control and bTi groups (Figure S2A, Supporting Information).

In addition to differences in cell area and aspect ratio, the nucleus area of the cells was also significantly decreased on all types of bTi as compared to flat Ti (Figure 3C). However, the trend was not similar to the cell spreading area. For instance, although the cells had a larger area on the Porous specimens as compared to the Partition specimens, the opposite was observed for the cell nucleus area.

The FAs formed at the periphery of the cells on the flat Ti, Partition, Porous, and Sparse specimens (Figure 2A). The average number of FAs per cell was significantly lower on all bTi specimens as compared to flat Ti (Figure 3D). The area of FA corresponding to flat Ti, Partition, and Sparse groups was on average 5.2 μm^2, which significantly decreased to 3.9 μm^2 in the Porous samples (Figure 3E). The bending of the pillars of the Partition and Sparse specimens beneath the cell body, especially at the directional zones where FAs are present, was observed in SEM images (**Figure 4**A). In addition, even though the majority of the FAs formed on all surfaces had an area of 2–6 μm^2, the cells residing on the Partition and Sparse samples formed some far larger FAs (Figure 4C). Furthermore, different cytoskeleton organization was observed. For the cells residing on the flat Ti and Porous specimens, clear actin stress fibers were formed, which were primarily oriented along the cell length (Figures 2A and 3F). This organization decreased on the Partition surfaces and almost disappeared on the Sparse surfaces.

2.3. Expression of Osteogenic Markers in Preosteoblast Cells

After 9 days of culture, immunocytochemical staining revealed the presence of Runx2 in the nuclear area of the cells residing on the surfaces of the flat Ti, Porous, and Partition specimens (**Figure 5**A). The average stained area per cell was not significantly different between those three groups (Figure 5B). However, no Runx2 was detected in the vicinity of the nuclei of the cells cultured on the surface of the Sparse specimens. Furthermore, after 14 days, significantly higher numbers of calcium depositions were formed in the matrix of the cells populating the surfaces of the Porous and Partition specimens as compared to those associated with the flat Ti and Sparse specimens (Figure 5A and Figure S2B, Supporting Information). The largest area of mineralized nodules belonged to the Partition specimens, which was significantly higher than all other groups. Porous surface was in the second place, while flat Ti and Sparse samples showed a lower capacity for inducing calcium deposition (Figure 5C).

2.4. Early Bactericidal Effects of bTi Surfaces

The live/dead staining of the adherent *S. aureus* bacteria after 18 h (**Figure 6**A,B) showed that all bTi surfaces had bactericidal activity, which increased from the Porous to the Partition and to the Sparse surfaces. On average, only 8% of the bacterial cells were found dead on flat Ti samples. The mean percentage of dead bacteria increased to 25 (SD 5%), 35 (SD 5%), and 42 (SD 7%) for the Porous, Partition, and Sparse specimens, respectively. The morphological evaluation of bacteria by SEM showed that they had a normal coccoid shape on flat Ti while they were stretched on the Porous specimens with a flattened morphology (Figure 6A). On Partition surfaces, stretching of the bacteria between adjacent pillars was even more visible. The penetration of the pillars into the cell wall was also detected, especially in the cells residing on top of the pillars (Figure 6A). The bacteria also bent the pillars underneath them (Figure 4B), which might impose additional mechanical forces to the bacterial cell wall.[49] The bacteria adhered to the Sparse specimens, were observed to be both stretched between the lateral sides of adjacent pillars and punctured by the sharp tips of the pillars (Figure 6A). The cells were even present in the interspaces between the clustered pillars as some of these spaces exceed the size of the bacteria (≈800 nm in diameter). Cells with normal morphology were hardly present on this type of surface. These findings were confirmed by the quantitative results of the CFU counting that showed that there is a significant difference between the flat Ti and bTi (Partition and Sparse) in terms of the number

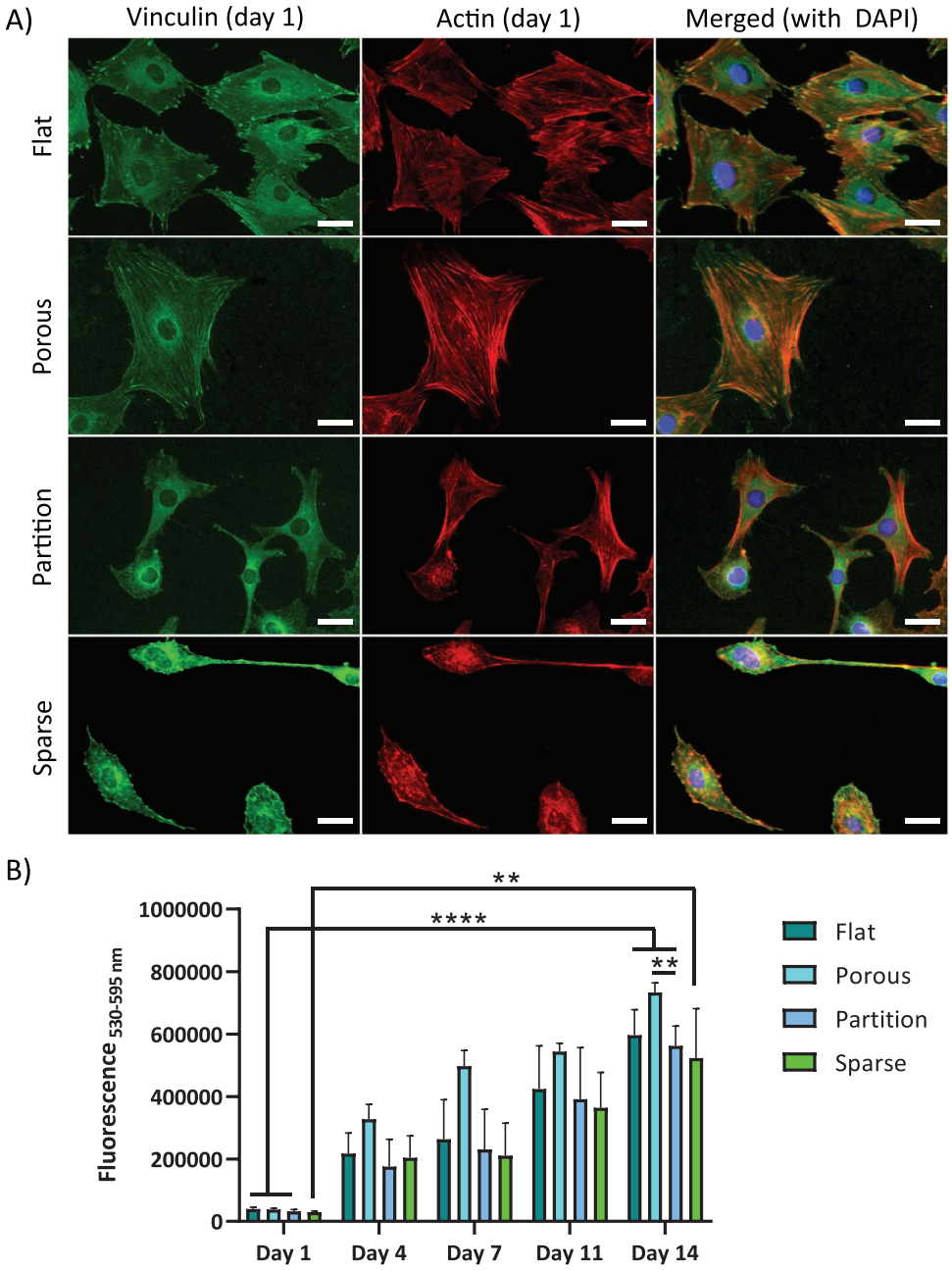

Figure 2. A) The immunocytochemical staining of vinculin (green), actin (red), and nucleus (blue, merged with the last two channels) for the MC3T3-E1 preosteoblast cells cultured on the flat Ti, Porous, Partition, and Sparse bTi specimens after 1 day. All surfaces except Sparse support the spreading of cells. Unlike the polygonal cell morphology on those samples, the majority of the cells are highly elongated on the Sparse specimens. Moreover, the colocalization of FAs and actin fibers can be detected in the Porous and Partition groups but not on the surface of the Sparse specimens. Scale bar = 30 µm. B) The metabolic activity of the preosteoblast cells cultured on the flat Ti and bTi surfaces measured by the PrestoBlue assay over 14 days. The increased metabolic activity of the cells with time indicates the cytocompatibility of all surfaces. ** $p < 0.01$, **** $p < 0.0001$.

of bacteria capable of forming a colony after being cultured on these samples (Figure 6C). As expected, none of the surfaces had an influence on the viability of non-adherent bacteria (Figure S2D, Supporting Information).

Moreover, performing the PrestoBlue assay at four different time points indicated that the bacterial metabolic activity is significantly lower on all bTi surfaces as compared to flat Ti at least after the first hour after culture (Figure 6D). This difference was also observed at 4, 8, and 18 h of culture. Comparing the different types of bTi, the metabolic activity of the bacteria increased until 4 h and then remained at the same level until 8 h after which it declined.

3. Discussion

Developing cell-instructive biomaterials could shift the paradigm in fabrication of orthopedic implants. The introduction

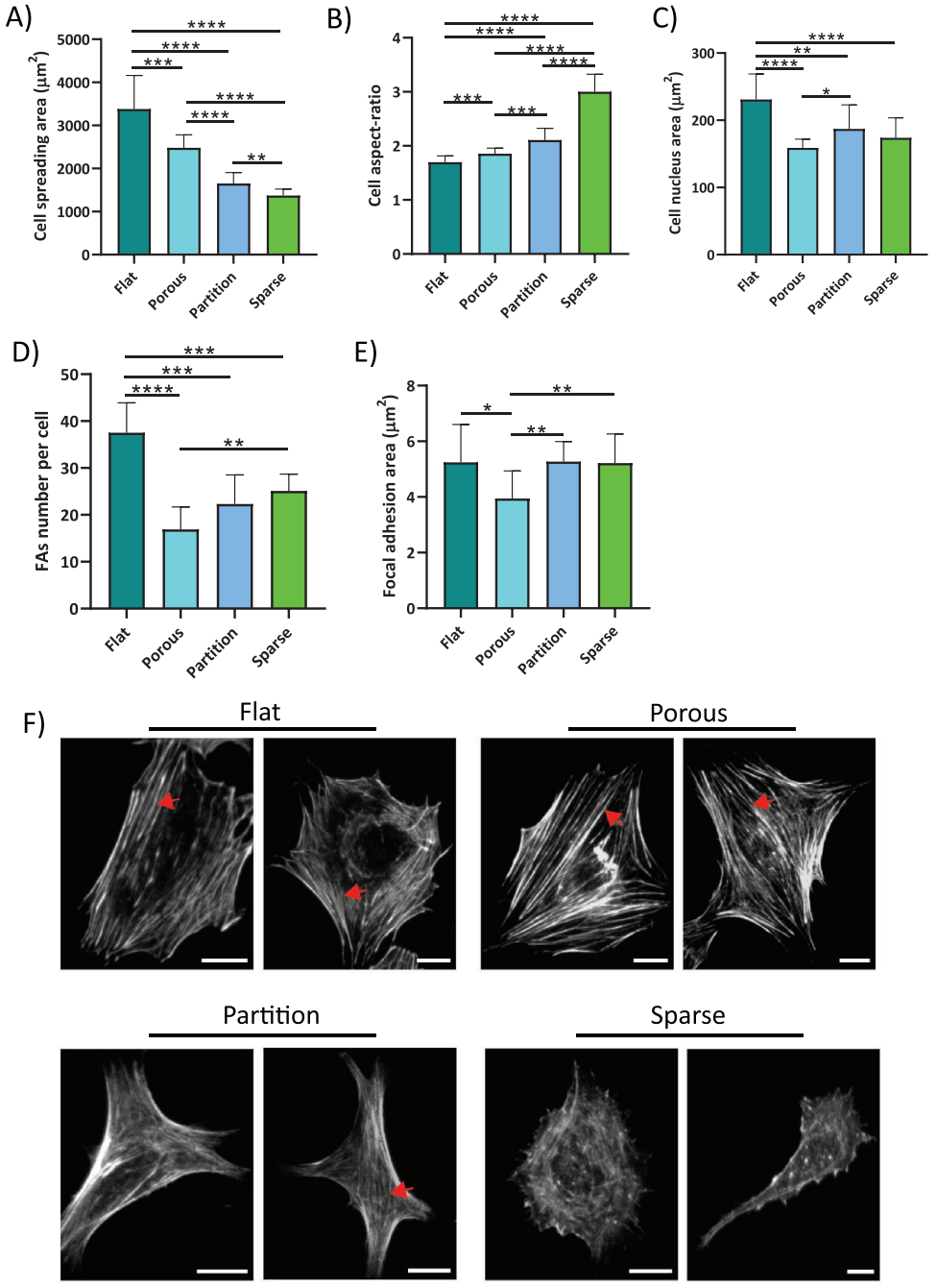

Figure 3. The morphological characteristics and early response of the preosteoblast cells cultured on the flat Ti and bTi surfaces after 1 day of culture. A) Spreading area. The cells spreading area significantly decreased for taller and more separated pillars. B) Cell aspect ratio. The elongation of the cells (i.e., their aspect ratio) gradually increased when going from the flat specimens to the Sparse specimens. C) Cell nucleus area. The cell nuclei were observed to be smaller on the bTi surfaces, especially in the case of the Porous group. Moreover, the fully rounded morphology of the nucleus on the surface of the Porous specimens slightly shifted to a more elongated morphology on the Partition and Sparse specimens (subfigure F). D) Number of focal adhesions per cell. Cells residing on bTi specimens formed significantly lower number of focal adhesions compared to the flat Ti (regardless of the type of topography). E) Focal adhesion area. The cells residing on the Porous bTi were found to form smaller FAs as compared to those inhabiting the surface of flat Ti and other types of bTi. * $p < 0.05$, ** $p < 0.01$, *** $p < 0.001$, **** $p < 0.0001$. F) The gray-scale images of the cytoskeleton. The organization of the cytoskeleton can be seen in the form of parallel actin fibers (shown by red arrows) on flat Ti and Porous bTi. Actin fibers appear to be partially organized in the case of the Partition specimens. No organization was observed in the case of the Sparse specimens. Scale bar = 20 μm.

of bactericidal bSi surfaces[45] drew attention to the use of (ICP) RIE for the fabrication of high aspect ratio pillars on the surface. Consequently, bactericidal bTi has been introduced as a promising biomaterial for preventing IAIs.[48] To date, numerous studies[46,47,50] have focused on the biological properties of bSi and bTi surfaces, trying to optimize the dimensions of the pillars

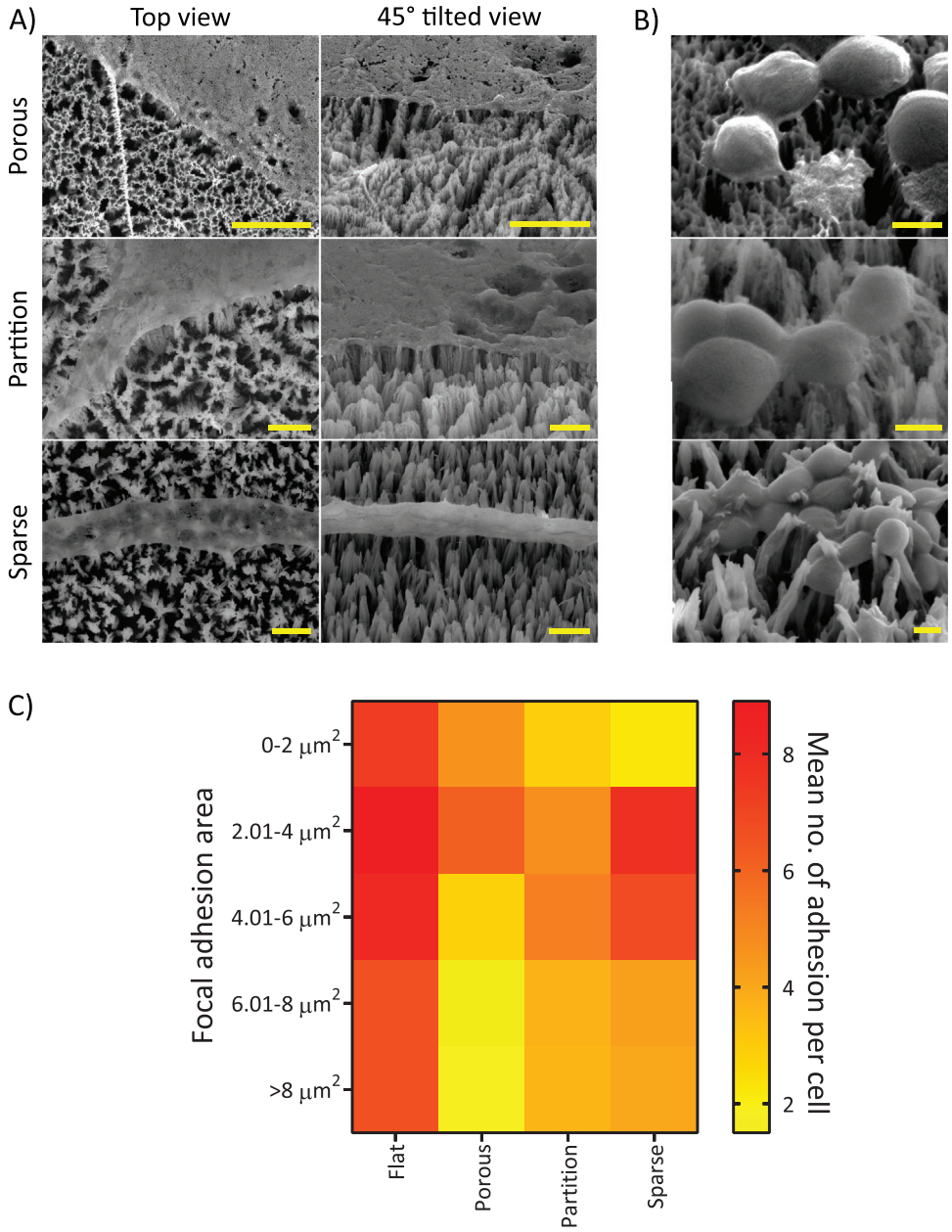

Figure 4. A closer look at the interaction of the preosteoblasts and bacterial cells with bTi surfaces. A) The top- and tilted-view SEM images of the directional regions of the preosteoblast cells. The cells can easily hold on to the abundant physical features present on the Porous surface as their anchorage points. On the Partition surfaces, it is not yet difficult to find enough anchorage points. The bending of the pillars can also be seen underneath the area in which FAs have been formed preferentially. The cells residing on the Sparse surfaces develop extremely long membrane extensions in search of more contact points. Scale bar = 2 μm. B) The interactions of *S. aureus* with the bTi surfaces. Scale bar = 500 nm. C) The heat map of the size distribution of FAs on the flat Ti and bTi surfaces.

by changing one single processing parameter (i.e., etching time). It was reported that fine changes in the characteristics of the such etched structures may influence their biological properties.[51] Yet a wider range of surfaces can be produced by taking advantage of other (ICP) RIE processing parameters.[44] Therefore, the optimum etched surfaces for a certain or multiple biofunctionality are yet to be established. Moreover, the literature offers limited data over the interactions of bTi surfaces with mammalian cells, especially those involved in the regeneration of bone tissue. Not much is known about the relationship between the early and long-term responses of the cells interacting with different bTi surfaces. Therefore, we tried to further explore the fabrication process (i.e., the chlorine-based maskless ICP RIE of Ti) and generate a couple of distinct bTi surfaces in an attempt to find a surface that provides the best dual-functionality (from both osteogenic and bactericidal points of view).

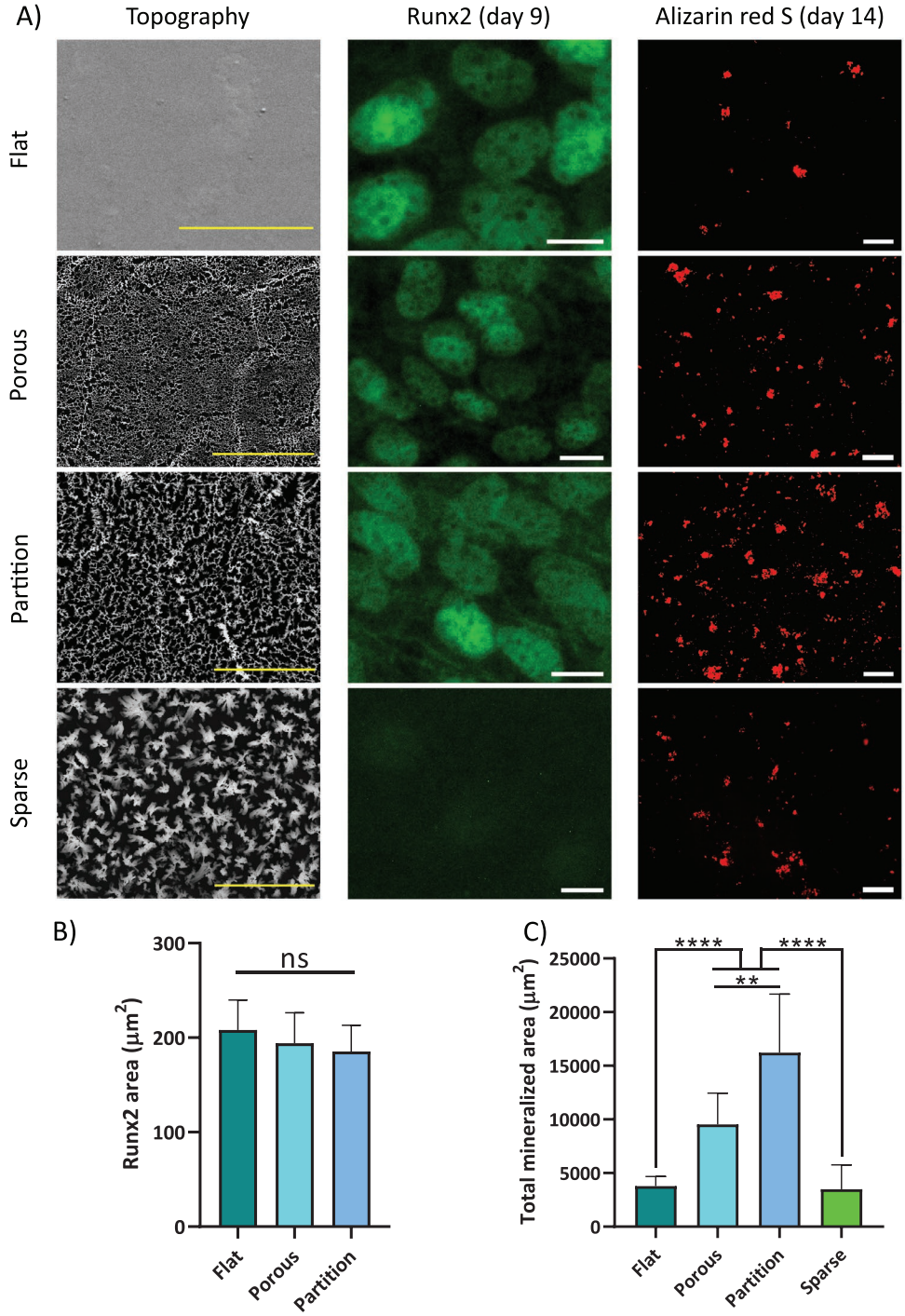

Figure 5. The long-term osteogenic response of the preosteoblast cells cultured on the flat Ti and bTi surfaces. A) The immunocytochemical staining of Runx2 and visualization of calcium deposits in the matrix by Alizarin red S assay after 9 and 14 days of culture, respectively. Scale bar = 5, 15, and 100 µm, for representative images of surface topographies, Runx2 and Alizarin red S, respectively. While the Porous and Partition bTi groups supported the expression of Runx2 as an early marker of osteogenic differentiation, the Sparse group inhibited it. B) Runx2 expression. Although the average stained area for Runx2 was significantly different between flat Ti, Porous, and Partition, the last two significantly increased C) the total mineralized area on the surfaces. Overall, the Partition bTi specimens showed the highest osteogenic potential among the different surfaces considered here. ** $p < 0.01$, **** $p < 0.0001$.

3.1. Looking at the Ti Pillars from a Physicochemical Perspective

Among the ICP RIE processing parameters, the temperature and pressure of the chamber are two variables that significantly impact the etching rate and morphology of the resulting structures.[44] At higher pressures, the energy of ions and radicals decreases as a result of increased number of collisions between them, which eventually decreases the etching rate (i.e., yields

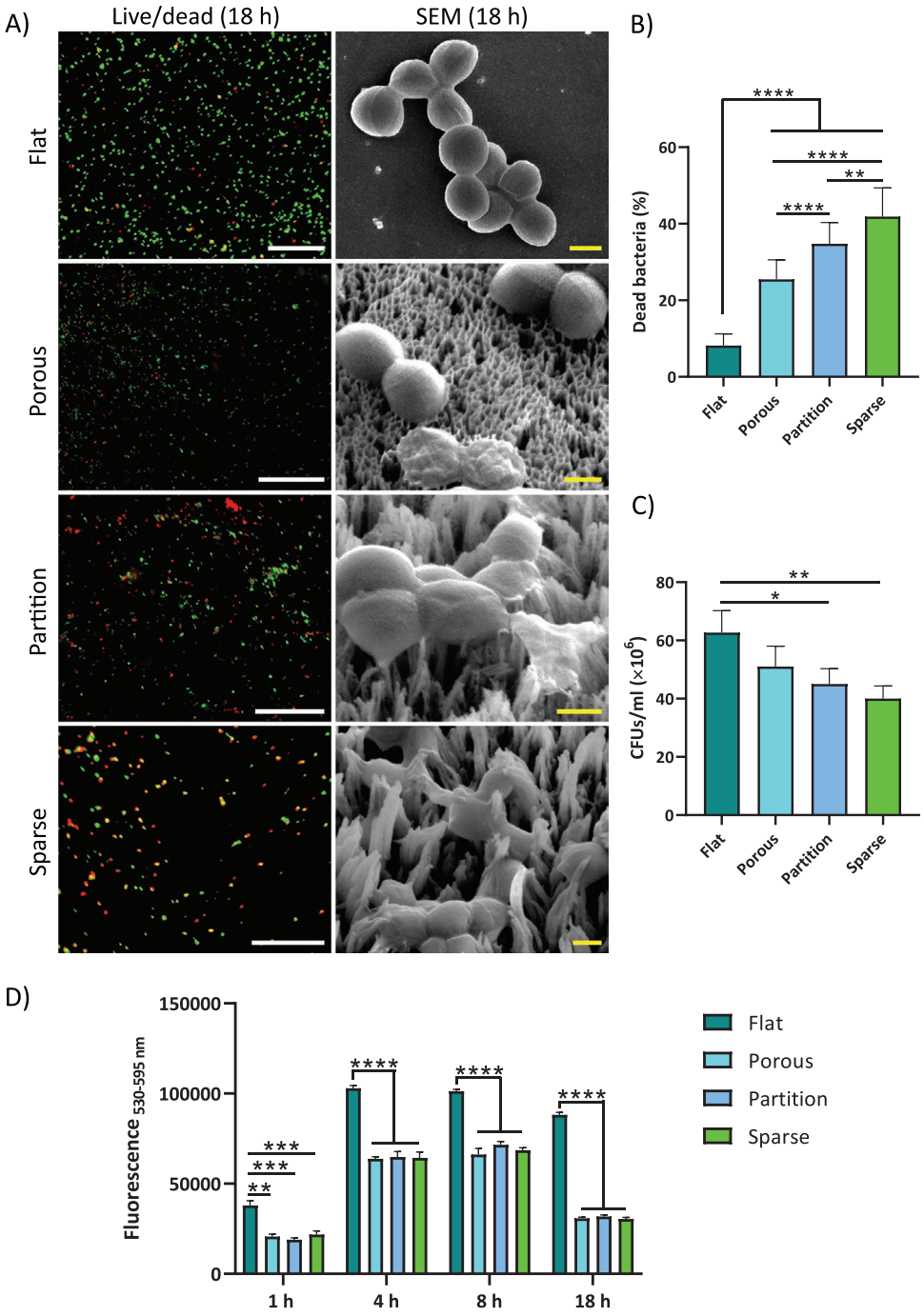

Figure 6. The bactericidal properties of flat Ti and bTi surfaces. A) The representative live/dead and SEM images of *S. aureus* cells cultured on surfaces for 18 h. Green and red cells indicate viable and dead bacterial cells in the live/dead images, respectively. While *S. aureus* has a normal coccoid shape on flat Ti, unusual flattened and ruptured morphologies were observed on the bTi surfaces. Scale bar = 20 µm and 500 nm for the live/dead and SEM images, respectively. B) The quantification of non-viable bacterial cells based on live/dead images. All surfaces exhibited killing efficiencies significantly higher than that of the flat surface, with the Sparse group being the most efficient antibacterial surface. C) The results of CFU counting showed a similar trend regarding the bactericidal properties of the bTi surfaces. D) The metabolic activity of the bacterial cells cultured on the flat Ti and bTi surfaces, measured by the PrestoBlue assay over 18 h. All the bTi surfaces significantly decreased the bacterial metabolic activity from the first hour of culture. At 4 h, higher metabolic activity was measured but it did not continue increasing. * $p < 0.05$, ** $p < 0.01$, *** $p < 0.001$, **** $p < 0.0001$.

shorter pillars for a constant etching time). Increasing the temperature enhances the etching rate of the sidewalls of the initially formed pillars, resulting in further separation and lower compactness of the pillars. By changing these two conditions, we generated surfaces with increased pillar heights and interspaces between the clustered pillars. These changes are,

however, not systematic as the height and interspace changed simultaneously in each bTi design. Yet, each surface was distinct from the rest by its unique combination of the height and organization of the pillars. Therefore, the biological properties of these surfaces should be associated with a combination of both of those parameters and not with the isolated effects of either. The height of the pillars increased from less than 400 nm to more than 1400 nm whereas the diameter was always less than 100 nm leading to an enhanced aspect ratio of the resultant structures. The interspace between the clustered/connected pillars also increased with the increase in height.

The chemical characterization of the bTi surfaces showed that the pillars mainly consist of Ti and O. The presence of an oxide layer on the surface has been confirmed by X-ray photoelectron spectroscopy analysis in other ICP RIE studies.[48,51] Furthermore, during the etching process, chlorine as the main etchant gas, the aluminum-made chamber wall, the quartz carrier wafer, and the organic solvents used for cleaning can respectively introduce negligible amounts of Cl, Al, Si, and C to the final etched Ti surface. Nevertheless, the bio-inertness of titanium is still preserved in form of TiO_x as the main component of the etched structures.[44]

All bTi surfaces used in this study were found to be superhydrophilic. The trend of the measured water contact angle of the surfaces was in line with a previous study[44] that showed that decreasing the temperature and, thus, the formation of more compact nanostructures leads to larger water contact angles as compared to the specimens fabricated at higher temperatures (e.g., 40 °C). Hasan et al.[48] have shown that the wettability of bTi enhances with an increased surface roughness. Similarly, the rougher samples in our study (Partition and Sparse) are the most hydrophilic surfaces. Yet the opposite trend in the relationship between wettability of bTi surfaces and the surface roughness in another study[51] suggests that the wettability model applicable to these types of surfaces is largely dependent on the dimensions of the pillars, as well as their interspacing.[52]

3.2. Adaptation of Preosteoblast Cells to bTi Surfaces

The results of this study together with other previous studies form a body of evidence to refute any possible cytotoxicity of bTi surfaces as long as the aspect ratio of the pillars remains below 20.[53,54] Based on the metabolic activity measurements and microscopic observations, preosteoblast cells could easily proliferate on all types of the bTi studied here. However, the cells varied in terms of their morphology and cytoskeleton organization, which influence the behavior of preosteoblasts as anchorage-dependent cells. Cells try to find as much suitable anchorage points as possible upon which the integrins can optimally bind to the protein ligands adsorbed on the surface.[29,55] On the Porous specimens, there are plenty of physical features that cells can reach onto without stretching their membrane extremely. This is starting to change on the Partition samples where cells need to develop membrane extensions in the form of filopodia to attach on the taller and partitioned pillars. The Sparse samples do not provide cells with close-enough features. Consequently, the cells tend to minimize their spreading area and keep connected via very long extensions leading to the elongated shapes observed.[55] The gradual increase in the aspect ratio of the cells from flat Ti to Sparse surfaces should, therefore, be considered in this context.

The formation of FAs and the global cytoskeletal remodeling via the formation of actin bundles play a crucial role in determining the ultimate cell fate.[56] Even the smallest surface features (2–4 nm in height) made of titanium have been shown to trigger a rapid reorganization of the cytoskeleton.[57] The mechanical forces exerted to the cells are transferred to the cell nucleus via the complex chains of integrins, FAs, and actin fibers, and then processed via different pathways and feedback loops. The analysis of FAs showed that by developing more directional protrusions in the cells residing on the Partition and Sparse specimens, FAs are regularly formed in the proximity of these polarized regions. This phenomenon is corroborated by previous studies that showed that the anisotropy of FAs distribution increases as the cell aspect ratio increases.[58,59] On the flat Ti, however, the formation of FAs could be detected at the periphery of the cells and also in the more internal regions of the cell body (closer to the cell nucleus). Moreover, on these surfaces, FAs were mainly oval-shaped and aligned with the actin fibers along their long axis (Figure 2A). The colocalization of FAs and actin fibers indicates the maturation of FAs and the establishment of a strong adhesion by coupling to the actin fibers (i.e., stable FAs with slow turnover rate).[55,60] On the contrary, the FAs of the cells residing on the Partition and Sparse specimens were relatively round and not yet mature. The colocalization of FAs and actin fibers is hardly recognizable on the Sparse samples. It can be assumed that short-lasting colocalization is another sign of a more migratory state in the cells residing on the Sparse specimens.[55] The actin fibers are well-oriented only inside the well-spread cells on the flat Ti and Porous specimens. On the other surfaces, the cells may be either already in the polarization phase or the contractile spreading phase, according to their morphology and cytoskeletal organization (Figures 2A and 3F).[61] In the contractile spreading phase, the actin bundles are still being formed and the cells intend to form strong adhesion to the surface. The abundant presence of filopodia in these cells and their smaller areas indicate such effort by the cells. It can, therefore, be concluded that the cells undergo a more difficult or slower adaptation to the Partition and Sparse surfaces as compared to the other surfaces.

3.3. FA-Mediated Mechanical Interactions with the Surface

The difference in the size of FAs (denoted by their area) on different surfaces may also indicate different levels of mechanical tensions exerted to the cells. The average size of FAs is significantly larger on the Partition, Sparse, and flat Ti groups as compared to the Porous specimens. That is likely because the cells struggle to effectively adhere to very smooth surfaces (e.g., flat Ti) or to highly separated pillars of the Sparse group, which is why they form larger FAs. The dynamic and force-dependent process of recruiting proteins, such as vinculin[62] to the FA sites is yet to be fully understood.[63] Not only could this process be cell type-dependent[11] but may also vary when studying the different types of surface topography and different culturing times.

For instance, similar to the results of this study, the MC3T3-E1 cells have been shown to form larger FAs on surfaces with increased pillar interspacing.[64] In comparison, hMSCs form larger FAs as their spreading area increases[65] while neuronal stem cells exhibit an increased expression of FAs (increasing the adhesion) on grooves and pillars with smaller interspacing as compared to their more separated counterparts.[66] Nevertheless, the variations in the size of FAs in this study indicate different local traction forces that the cells exert to the pillars. It has been shown that although a correlation between the size of FAs and traction forces exists during the initial stages of adhesion, the same does not apply to mature adhesions.[67] In other words, mature FAs can withstand extremely increased tensions (up to sixfold) without any changes in their size. As described above, the FAs of cells residing on the Porous samples are mature long-lasting ones while the FAs present on the surface of the Sparse specimens are rather nascent adhesions. Moreover, super-resolution imaging has shown that some of the studies that had concluded such correlations between the size of FAs and the generated force, had, in fact, considered multiple small adhesions as a large adhesion.[68] The further evaluations of the adhesion forces using novel AFM-based methods and computational analysis are necessary to improve our understanding of FA-mediated mechanical interactions of cells with such pillars.[69]

The size and distribution of FAs also affect the nuclear morphology and remodeling as the nuclear dynamics are controlled by the tensions that are exerted at the adhesion points and propagate through the actin fibers to their nuclear cap.[70,71] It has been argued that applying higher tensions to the cell nuclei via smaller FAs, which are unevenly distributed and, therefore, stretch the nuclei to some extent, enhances the osteogenic differentiation.[71] In our study, heterogeneous distribution of FAs in Partition and Sparse samples has changed the fully rounded morphology of cell nuclei in many cells toward a more elongated morphology (Figure 3F). The changes in the size and orientation of nuclei together with the forces exerted via FAs may explain the long-term osteogenic response of the cells on the different surfaces.

3.4. Osteogenic Properties of bTi from a Mechanotransduction Perspective

The mechanotransduction pathways by which the environmental mechanical stimuli cause alterations in the expression of certain genes and the transcription of their correspondent proteins have been spotlighted but are not completely understood yet. A plethora of subcellular components is involved in these processes starting from the integrins bound to the membrane and continuing all the way to the inside of the nucleus. For instance, focal adhesion kinase (FAK) is known to play a vital role in the regulation of other components and can trigger a lot of such intracellular pathways.[63,72] FAK is associated with the β-subunit of integrins, especially the β1 subunit and is able to promote the expression of Runx2 via the FAK/extracellular signal-regulated kinase pathway[73] and also by triggering the mitogen-activated protein kinases cascade.[16,74] It has been shown that in MSCs cultured on a variety of surfaces, Runx2 expression is correlated with the reinforcement of FAs.[75] The results of Runx2 staining in our studies can be perceived accordingly. Unlike the flat Ti, Porous, and Partition groups, perinuclear Runx2 was not detected in the Sparse group where there was no cytoskeleton organization and FAs were less stable. FAK is also regarded as the upstream of RhoA activation, which affects cell contractility, spreading, and eventually the osteogenic differentiation of MSCs via the RhoA/ROCK pathway.[16] Our results suggest that the inhibition of FAK phosphorylation could be the reason for the downregulation of Runx2 in the Sparse samples. Nevertheless, further studies are required to examine this hypothesis. The analysis of calcium deposits in the matrix after 2 weeks of culture revealed that Porous and Partition surfaces highly enhance matrix mineralization as compared to flat Ti. Although an increased number of FAs is generally considered beneficial for osteogenesis,[76] our findings highlight the importance of surface topography as Porous surface is significantly more osteogenic than flat Ti despite its fewer and smaller FAs. The higher potential of Partition as compared to Porous might also be associated with the different levels of cell spreading and contractility, which influences mechanotransduction pathways more in favor of osteogenesis on the Partition surfaces. A bTi surface consisting of high aspect ratio pillars with a second tier of shorter pillars has been recently shown to increase the calcium deposition in the matrix of human adipose-derived stem cells (hASCs).[54] Similar to our findings, hASCs had formed fewer FAs as compared to polished titanium samples.[54] Another important intracellular signaling pathway to consider is Yes-associated protein (YAP)/transcriptional coactivator with PDZ-binding motif (TAZ). A higher percentage of YAP localized in the cell nucleus has been shown to be related to an increased formation of FAs and cell tension.[76] Further dedicated experiments are needed to answer questions about the specific role of integrins, mechanotransduction pathways, and culture conditions[77] in the expression of late osteogenic markers induced by bTi surfaces.

In summary, not fully-separated Ti pillars with an approximate height between 700 and 1000 nm showed the highest potential for inducing matrix mineralization in preosteoblasts. This may be associated with the changes in cell morphology and strong attachment to the surface facilitated by stable FAs. It is noteworthy that the findings related to the adaptation and the osteogenic response of cells in this study cannot be necessarily generalized to other cell types, such as primary osteoblasts or hMSCs. Further independent studies are required to elucidate the specific responses of those cells to bTi surfaces.

3.5. Early Interactions of Bacteria with bTi

Bactericidal properties are one of the core values of RIE-modified surfaces. The commonly accepted theories regarding the early stage interactions of the bacteria with such surfaces have been explained previously.[42] In the present study, no signs of pillar penetration were observed in the *S. aureus* bacteria interacting with the Porous specimens as all the pillars were connected to each other at their tips. Still, bacteria stretched their cell envelope to be able to find anchorage points on the surface (Figure 4B). While 25 ± 5% of the adhered bacteria were dead

on the Porous specimens, the percentage of the dead bacteria reached its peak (42 ± 7%) for the Sparse group where a combination of the direct penetration of the pillars into the cell wall, the bending of the pillars, the stretching of the cell wall between adjacent pillars, and the sliding down between the pillars were observed (Figure 4B). The killing efficiency of these bTi surfaces is expected to be even higher against Gram-negative bacteria such as *E. coli* and *P. aeruginosa* due to their thinner cell wall and rod-shaped morphology that increase their susceptibility to the sharp tips of the pillars.[24,45,46] Although the killing efficiency of the Sparse specimens against *S. aureus* is similar to Ti etched for 10 min in the study by Linklater et al.,[51] higher killing efficiencies have been also reported for both bSi and bTi, in which the height and arrangement of the pillars are comparable to the Sparse group.[48,53] It is noteworthy that the killing efficiency of a surface could vary against different strains of a species due to the differences present in the strain-dependent characteristics of the cells including their motility.[78]

It has been shown that the number of dead *S. aureus* cells on bTi surfaces significantly increases over time (from ≈20% after 4 h to more than 75% after 24 h).[48] A similar conclusion can be made for our experiments. The metabolic activity of the bacterial cells attached to bTi surfaces is significantly lower than those attached to the flat Ti at any time point. However, comparing the metabolic activity of bacterial cells within the bTi groups, it increases up to 4 h and then decreases therefrom. It might confirm that the first 4 h is the window of opportunity within which bactericidal topographies can inhibit bacterial colonization on the surface. We cannot, however, attribute the decreased metabolic activity solely to the death of bacterial cells. Assuming that the different types of bTi surfaces in this study exert forces of different magnitudes to the bacterial cells, it would be expected that different signaling pathways may come into play and regulate the cell adhesion, motility, metabolic activity, genomics, and proteomics of the bacteria.[79–82] Further studies are required to scrutinize the killing mechanisms of such surfaces by using a mechanistic approach.

Overall, comparing the responses of the preosteoblast cells and bacteria to that of the bTi surfaces investigated in this study showed that the Partition surfaces with a pillar height of 700–1000 nm and a partially-separated organization exhibit both bactericidal and osteogenic properties. Such a surface was capable of killing a significant percentage of the adherent bacteria while promoting the osteogenic response of cells. These observations suggest that achieving a specific design with balanced bactericidal and osteogenic properties is possible within the capabilities of ICP RIE. In summary, etching the titanium surfaces for 10 min with a combination of Cl_2 and Ar gasses (flow rates: 30 and 2.5 sccm, respectively), at a high temperature (i.e., 40 °C), and under a moderate chamber pressure (i.e., 2.0 Pa) produces pillars with differential effects on the bacteria and mammalian cells.

4. Conclusion

In summary, we investigated the dual-functionality of a series of bTi surfaces as well as the possible mechanisms behind those functionalities. Superhydrophilic etched Ti surfaces containing pillars with distinct heights and spatial organization were produced by changing the pressure and temperature of the chamber during the ICP RIE process. Although all groups of the modified Ti surfaces studied here were cytocompatible for the MC3T3-E1 preosteoblast cells, they induced significantly different cell shapes, area, aspect ratio, nucleus area, cytoskeletal organization, patterns of FA formation, and the extent of matrix mineralization. When the pillars were very tall and separated (i.e., Sparse surfaces), the cells possessed the least area possible and exhibited extremely elongated shapes. Moreover, the actin fibers were no longer well-oriented and the colocalization of FAs and actin fibers was lost. On the other hand, on the Porous and Partition surfaces, the cells were well-spread with polygonal shapes. More stable FAs indicated that they may have more intensively transduced the forces exerted to the cells to the nuclei, improving the matrix mineralization most probably by triggering FAs-mediated mechanotransduction pathways. Bacteria responded differently to these surfaces too. Sparse surfaces showed the highest killing efficiency against the bacteria. A combination of direct penetration of the pillars into the cell wall and cell wall stretching between adjacent pillars was observed in this group. Overall, the results of this study show that various ICP RIE conditions can be used to create Ti surfaces that are capable of instructing mammalian cells while killing bacteria. Based on our findings, the Partition surfaces establish a balance between osteogenic and bactericidal properties, which makes it a good candidate for further studies in vivo as a prerequisite for its final use in clinical settings.

5. Experimental Section

Fabrication and Characterization of bTi Samples—Fabrication: Annealed titanium foils with a thickness of 125 µm (99.96% purity, Goodfellow, UK) were cut to the size of a 4-inch (diameter = 10.2 cm) silicon wafer and were polished by chemical-mechanical polishing (CMP Mecapol E460, Saint-Martin-le-Vinoux, France). The surface was then coated with a photoresist to protect it against damages. The titanium wafer was further cut into 8 × 8 mm^2 pieces using a Disco dicer (Disco Hi-Tec Europe GMbH, Germany). The photoresist layer was subsequently removed by acetone and the samples were cleaned in ethanol and isopropyl alcohol (IPA). The samples were spin-dried prior to surface modification by ICP RIE. An ICP RIE machine (PlasmaLab System 100, Oxford Instruments, UK) was used to create three types of structures on the titanium surface, which were distinct in terms of their morphological parameters and organization. Therefore, the polished samples were glued with diffusion oil on a 4-inch quartz wafer as the carrier wafer. The etching process was performed with Cl_2 and Ar gases while the pressure of He (i.e., the back-cooling gas) was kept at 1066 Pa. The following processing parameters were the same for all three types of modified surfaces: ICP source power = 600 W, RF power = 100 W, etching time = 10 min, Cl_2 flow rate = 30 sccm, and Ar flow rate = 2.5 sccm. However, the temperature and pressure of the chamber were changed for each type of surface as follows: 0 °C and 4.0 Pa for the first group, 40 °C and 2.0 Pa for the second condition, and 40 °C and 0.5 Pa for the third condition. Following the etching process, the samples were cleaned in acetone, ethanol, and IPA, respectively (each step lasted 30 min), and were then spin-dried for further characterization and experiments.

Morphological Characterization: The etched surfaces were imaged by SEM (Helios NanoLab 650, FEI, US). Top and tilted view (35°) images were acquired at different magnifications to assess the morphology and spatial organization of the resultant pillars. The mean roughness (R_a) and root mean squared roughness (R_q) were also estimated for each

sample as the mean ± SD of the values measured for three images of 100 μm² each by AFM (JPK Nanowizard 4, Bruker, Germany) using a high aspect ratio probe (TESPA-HAR, Bruker, Germany) in the tapping mode.

Surface Chemical Composition: The elemental chemical composition of the surfaces was determined using energy-dispersive X-ray spectroscopy (EDS) performed inside the SEM (Helios Nanolab 650, FEI, US). The major chemical elements were identified from the EDS spectra.

Surface Wettability: The wettability of the flat Ti surface (i.e., polished, non-treated Ti surfaces) and bTi surfaces were evaluated by measuring the static water contact angle in duplicate using a drop shape analyzer (DSA 100, Kruss, Germany). A volume of 1.5 μL deionized water with a falling rate of 60 μL min^{-1} was placed on the surface using a syringe. The images were recorded after 5 s.

Preosteoblast Cell Response to bTi Surfaces—Pre-Culture of Cells and Cell Seeding: Preosteoblast MC3T3-E1 cells (Sigma Aldrich, Germany) were cultured in alpha minimum essential medium (α-MEM) supplemented with 10% (v/v) fetal bovine serum and 1% (v/v) penicillin-streptomycin (all from Thermo Fisher Scientific, US). The medium was refreshed every 2 days. The samples were sterilized by immersion in 70% ethanol and exposure to UV light for 20 min. Upon reaching confluence, cells were detached from the cell culture flask using 1X trypsin-EDTA solution (Thermo Fisher Scientific, US) and were cultured on both flat Ti and bTi surfaces (2×10^4 cells per sample) in a 48 well-plate (Greiner, Bio-One, The Netherlands), and were incubated at 37 °C and 5% CO_2 (Life Technologies, US). This cell culture procedure was followed for all the cell experiments described in the following sections. In the case of experiments taking longer than 1 day, the medium was supplemented with 50 μg mL^{-1} ascorbic acid (1:1000) and 4mM β-glycerophosphate (1:500) (both from Sigma Aldrich, Germany) from day 2 onward. All experiments, described in the following sections, were independently performed two times, each time in quadruplicates.

PrestoBlue Assay: The metabolic activity of the cells seeded on flat Ti and bTi surfaces was measured by a PrestoBlue assay after 1, 4, 7, 11, and 14 days of culture. Therefore, all surfaces ($n = 4$ per group) were incubated in 250 μL α-MEM supplemented with 25 μL PrestoBlue reagent (Thermo Fisher Scientific, US) for 1 h at 37 °C and 5% CO_2. Thereafter, 100 μL of the supernatant from each well was transferred to a 96 well-plate (Greiner, Bio-One, The Netherlands) in duplicate. The fluorescence was measured at an excitation wavelength of 530 nm and an emission wavelength of 595 nm with a Victor X3 microplate reader (PerkinElmer, Groningen, The Netherlands).

Immunocytochemical Analysis of Preosteoblast Cells: In order to evaluate the short-term response of these cells to bTi surfaces and their morphological changes, the actin filaments, nucleus, and FAs of the cells were stained after 1 day of culture. The specimens were first washed twice with 10X PBS (Sigma Aldrich, Germany) and the cells were fixated using a 4% (v/v) formaldehyde solution (Sigma Aldrich, Germany). The cell membrane was permeabilized by adding 0.5% Triton X-100/PBS (Sigma Aldrich, Germany) at 4 °C for 5 min and then the samples were incubated in 1% BSA/PBS (Sigma Aldrich, Germany) at 37 °C for 5 min. Subsequently, the samples were incubated in anti-vinculin mouse monoclonal primary antibody (1:100 in 1% BSA/PBS, Sigma Aldrich, Germany) and rhodamine-conjugated phalloidin (1:1000 in 1% BSA/PBS, Thermo Fisher Scientific, US) for 1 h at 37 °C. The cells were then washed three times (5 min each time) with 0.5% Tween-20/PBS (Sigma Aldrich, Germany) before being incubated in Alexa Fluor 488, donkey anti-mouse polyclonal secondary antibody (1:200 in 1% BSA/PBS, Thermo Fisher Scientific, US) for 1 h at room temperature. The specimens were washed again three times with 0.5% Tween-20/PBS (5 min each time), followed by 5 min washing with 1X PBS. To simultaneously visualize the cell nuclei and properly mount the samples on microscopic glass slides, 10 μL Prolong gold antifade reagent containing DAPI (4′,6-diamidino-2-phenylindole) (Thermo Fisher Scientific, US) was laid on the surfaces and then five different locations of each sample were imaged using a fluorescence microscope (ZOE fluorescent cell imager, Bio-Rad, The Netherlands). For the SEM observations, the stained samples were washed twice with distilled water for 5 min and then dehydrated in 50%, 70%, and 96% ethanol solutions for 15, 20, and 20 min, respectively. Eventually, the samples were dried overnight at room temperature and were gold-sputtered before SEM imaging.

Investigation of the Osteogenic Properties of bTi Surfaces: To investigate the long-term osteogenic response of preosteoblast cells, the expression of some of the early and late osteogenic markers (i.e., Runx2 and calcium deposits) was studied.

For immunocytochemical staining of Runx2 (at day 9 of culture), a procedure similar to the previous section was followed. After fixation and permeabilization, the cells were incubated in recombinant anti-Runx2 rabbit monoclonal primary antibody (1:250 in 1% BSA/PBS, Abcam, UK). The cells were then incubated in Alexa Fluor 488, donkey anti-rabbit polyclonal secondary antibody (1:200 in 1% BSA/PBS, Thermo Fisher Scientific, US). Washing, mounting, imaging, and dehydration processes were followed similarly as described above.

Alizarin red S staining was performed on day 14 of culture to assess the deposition of calcium in the cells' matrix. Briefly, cells were washed and fixated as described above. The specimens were then incubated in 2% (w/v) Alizarin red S solution (Sigma Aldrich, Germany) for 30 min in the dark. The specimens were then rinsed five times with distilled water before being imaged by a ZOE fluorescent cell imager (Bio-Rad, The Netherlands) (five different locations of the surface).

Fluorescent Image Analysis: ImageJ 1.53c (NIH, US) and FA analysis server[83] were used to extract and quantify data from the fluorescent images. Each image overlay was split into separate channels for further evaluation of the nucleus, F-actin, and other proteins (i.e., vinculin). By thresholding the grayscale images of F-actin and vinculin, the cell spreading area, cell nucleus area, and the number and area of FAs were quantified through the Analyze Particles command. By fitting ellipses to the cell area, the minor and major diameters were measured and used to determine the aspect-ratio of the cells. A previously described method[84] was used to quantify the number and area of FA (for fully separated ones). Briefly, for 15 cells per study group, the background was subtracted from the greyscale images under the Sliding Paraboloid option with a rolling ball radius of 50 pixels. The local contrast of the image was then enhanced by running the CLAHE plugin with a block size of 19, histogram bins of 256, and a maximum slope of 6. To further minimize the background, the mathematical exponential function (EXP) was applied through the process menu. Thereafter, the brightness, contrast, and threshold were automatically adjusted before measurements using the Analyze Particles command. Similar image processing was performed to quantify the expression of Runx2. The number of mineralized nodules and their total area on the surface was quantified by running the Analyze Particles command on the images of Alizarin red S assay.

Bacterial Studies—Preparation of Bacterial Cultures: Gram-positive *S. aureus* bacteria (RN0450 strain) (BEI Resources, US) were grown on brain heart infusion (BHI) (Sigma Aldrich, US) agar plates at 37 °C overnight. A pre-culture of bacteria was prepared by inoculating a single colony in 10 mL autoclaved BHI, shaken at 140 rpm at 37 °C. The bacterial cells were collected at their logarithmic stage of growth and the optical density of the inoculum at 600 nm wavelength (OD_{600}) in the medium solution was first measured by a WPA Biowave II spectrophotometer (Biochrom, UK) and was then adjusted to a value of 0.1 (equivalent to 4×10^8 CFU mL^{-1}) to be cultured on the flat Ti and bTi surfaces. All surfaces were sterilized by immersion in 70% ethanol and exposure to UV light for 20 min. 250 μL of the bacterial inoculum was added to each surface in a 48 well-plate (Cell Star, Germany) (i.e., 10^8 CFU per sample). All experiments, described in the following sections, were independently performed two times, each time in triplicate.

Bacterial Metabolic Activity (PrestoBlue Assay): To follow the metabolic activity of the adherent bacterial cells seeded on flat Ti and bTi surfaces, the PrestoBlue assay was performed at 1, 4, 8, and 18 h of culture, using the same replicates for all the time points. At each time point, all surfaces were incubated in 250 μL of BHI broth supplemented with 25 μL PrestoBlue cell viability reagent (Thermo Fisher Scientific, US) for 1 h at 37 °C. Thereafter, 100 μL of the medium from each well was

transferred to a 96 well-plate (Cell Star, Germany) in duplicate. The fluorescence was measured at an excitation wavelength of 530 nm and an emission wavelength of 595 nm using a Synergy 2 microplate reader (BioTek, US).

Furthermore, to visualize the morphological state of bacterial cells on the surfaces and investigating the interactions between bacteria and surfaces, the specimens were imaged by SEM after 18 h of culture. To this end, the adhered bacterial cells were fixated by immersion in a PBS solution containing 4% formaldehyde and 1% glutaraldehyde (both from Sigma Aldrich, US) at 4 °C for 1 h. Subsequently, the samples were dehydrated by washing with MilliQ water for 10 min, 50% ethanol for 15 min, 70% ethanol for 20 min, and 96% ethanol for 20 min, respectively. Eventually, they were soaked in hexamethyldisilazane (Sigma Aldrich, US) for 30 min. After being air-dried, a thin layer of gold was sputtered on the samples before imaging by SEM at different magnifications and the tilt angles of 0° and 45°.

Live/Dead Staining: To investigate the bactericidal properties of the surfaces, the live/dead staining of the adhered bacteria was performed using L7012 Live/Dead *Bac*Light Bacterial Viability Kit (Invitrogen, US) after 18 h of culture according to the manufacturer's instructions.[44] Briefly, the non-adherent bacteria were removed by removing the medium from wells. The samples were then washed twice by 0.85% (w/v) NaCl solution. Subsequently, the adherent bacteria were stained by a 1:1 mixture of SYTO 9 green-fluorescent and propidium iodide red-fluorescent stains for 15 min at room temperature to distinguish between the live and dead bacteria based on their membrane integrity. Following the staining, the samples were rinsed again with 0.85% (w/v) NaCl solution and were then imaged (magnification: 20×) by a Luca R 604 widefield fluorescence microscope (Andor Technology, UK). Five different areas of each sample were imaged and the number of live and dead bacteria was quantified using the ImageJ Analyze Particles command. The percentage of the dead cells per surface was reported as the killing efficiency of the surface.

CFU Counting: CFU counting was performed as a complementary method to compare the bactericidal properties of flat Ti and bTi surfaces. After 18 h of culture, the supernatant BHI broth was collected to quantify the number of non-adherent bacterial cells. 100 µL aliquots of tenfold serial dilutions were plated on BHI agar plates and CFUs were manually counted after overnight incubation at 37 °C. On the other hand, the bacterial cells adhered to each sample were collected by sterile cotton swabs and were ultrasonicated in 1 mL PBS for 15 min using an Elmasonic S 30 ultrasonic cleaning unit (Elma Schmidbauer GmbH, Germany). The detached bacterial cells were plated on Petrifilm aerobic count plates (3M, US) and were incubated at 37 °C overnight. The red dots appeared on the petrifilms as indicators of viable cells were manually counted.

Statistical Analysis: For all of the above-mentioned experiments, the raw data were first tested for normal distribution using the D'Agostino-Pearson omnibus normality test in Prism version 8.4.3 (GraphPad, US). In the cases where the sample size was too small for such a test, the Shapiro–Wilk normality test was performed. The Brown–Forsythe and Welch ANOVA test was then performed, followed by the Dunnett's T3 multiple comparisons test to determine the statistical significance of the differences between the means of the different experimental groups. Since the results of the surface wettability and Runx2 staining experiments were found to be not normally distributed, the non-parametrical Kruskal–Wallis test was performed, followed by the Dunn's multiple comparisons test. In addition, the results of the PrestoBlue assay for both mammalian and bacterial cells were analyzed using the two-way ANOVA test, followed by the Tukey's multiple comparisons *post-hoc* analysis. A *p*-value below 0.05 was considered to indicate statistical significance.

Supporting Information

Supporting Information is available from the Wiley Online Library or from the author.

Acknowledgements

This research has received funding from the European Research Council under the ERC grant agreement No. [677575]. The authors would like to thank Dr. Bram van der Eerden (Department of Internal Medicine, Erasmus MC) for critically reading the manuscript and Dr. Cornelis W. Hagen (Department of Imaging Physics, TU Delft) for the access to the SEM equipment.

Conflict of Interest

The authors declare no conflict of interest.

Data Availability Statement

The data that support the findings of this study are available from the corresponding author upon reasonable request.

Keywords

antibacterial effects, cell morphology, focal adhesions, osteogenic response, reactive ion etching, synthetic bone substitutes

Received: February 3, 2021
Revised: March 24, 2021
Published online: May 12, 2021

[1] A. Falco, M. Berardini, P. Trisi, *Int. J. Oral Maxillofac. Implants* **2018**, *33*, 824.
[2] I. C. Chou, S. Y. Lee, C. P. Jiang, *Int. J. Numer. Methods Biomed. Eng.* **2014**, *30*, 1223.
[3] R. Hedayati, M. Sadighi, M. Mohammadi-Aghdam, A. Zadpoor, *Int. J. Mech. Sci.* **2016**, *106*, 19.
[4] E. García-Gareta, M. J. Coathup, G. W. Blunn, *Bone* **2015**, *81*, 112.
[5] A. Barradas, H. Yuan, C. A. van Blitterswijk, P. Habibovic, *Eur. Cells Mater.* **2011**, *21*, 407.
[6] A. L. Overmann, C. Aparicio, J. T. Richards, I. Mutreja, N. G. Fischer, S. M. Wade, B. K. Potter, T. A. Davis, J. E. Bechtold, J. A. Forsberg, D. Dey, *J. Orthop. Res.* **2020**, *38*, 1445.
[7] C. R. Arciola, D. Campoccia, L. Montanaro, *Nat. Rev. Microbiol.* **2018**, *16*, 397.
[8] A. Trampuz, A. F. Widmer, *Curr. Opin. Infect. Dis.* **2006**, *19*, 349.
[9] U. Filipović, R. G. Dahmane, S. Ghannouchi, A. Zore, K. Bohinc, *Adv. Colloid Interface Sci.* **2020**, *283*, 102228.
[10] L. Li, J. Eyckmans, C. S. Chen, *Nat. Mater.* **2017**, *16*, 1164.
[11] K. Anselme, P. Davidson, A. Popa, M. Giazzon, M. Liley, L. Ploux, *Acta Biomater.* **2010**, *6*, 3824.
[12] M. M. Stevens, J. H. George, *Science* **2005**, *310*, 1135.
[13] H. Amani, H. Arzaghi, M. Bayandori, A. S. Dezfuli, H. Pazoki-Toroudi, A. Shafiee, L. Moradi, *Adv. Mater. Interfaces* **2019**, *6*, 1900572.
[14] D. Baptista, L. Teixeira, C. van Blitterswijk, S. Giselbrecht, R. Truckenmüller, *Trends Biotechnol.* **2019**, *37*, 838.
[15] X. Zhao, L. Jin, H. Shi, W. Tong, D. Gorin, Y. Kotelevtsev, Z. Mao, *Colloid Interface Sci. Commun.* **2020**, *35*, 100249.
[16] K. Metavarayuth, P. Sitasuwan, X. Zhao, Y. Lin, Q. Wang, *ACS Biomater. Sci. Eng.* **2016**, *2*, 142.
[17] N. Logan, P. Brett, *Stem Cells Int.* **2013**, *2013*, 361637.
[18] G. Abagnale, M. Steger, V. H. Nguyen, N. Hersch, A. Sechi, S. Joussen, B. Denecke, R. Merkel, B. Hoffmann, A. Dreser, *Biomaterials* **2015**, *61*, 316.

[19] M. Croes, S. Bakhshandeh, I. van Hengel, K. Lietaert, K. van Kessel, B. Pouran, B. van der Wal, H. Vogely, W. Van Hecke, A. Fluit, *Acta Biomater.* **2018**, *81*, 315.
[20] A. Panáček, L. Kvítek, M. Smékalová, R. Večeřová, M. Kolář, M. Röderová, F. Dyčka, M. Šebela, R. Prucek, O. Tomanec, *Nat. Nanotechnol.* **2018**, *13*, 65.
[21] S. B. Levy, B. Marshall, *Nat. Med.* **2004**, *10*, S122.
[22] H. S. Azevedo, I. Pashkuleva, *Adv. Drug Delivery Rev.* **2015**, *94*, 63.
[23] S. Dobbenga, L. E. Fratila-Apachitei, A. A. Zadpoor, *Acta Biomater.* **2016**, *46*, 3.
[24] K. Modaresifar, S. Azizian, M. Ganjian, L. E. Fratila-Apachitei, A. A. Zadpoor, *Acta Biomater.* **2019**, *83*, 29.
[25] D. V. Iwamoto, D. A. Calderwood, *Curr. Opin. Cell Biol.* **2015**, *36*, 41.
[26] N. C. Gauthier, P. Roca-Cusachs, *Curr. Opin. Cell Biol.* **2018**, *50*, 20.
[27] T. D. Ross, B. G. Coon, S. Yun, N. Baeyens, K. Tanaka, M. Ouyang, M. A. Schwartz, *Curr. Opin. Cell Biol.* **2013**, *25*, 613.
[28] Y. Hou, W. Xie, L. Yu, L. C. Camacho, C. Nie, M. Zhang, R. Haag, Q. Wei, *Small* **2020**, *16*, 1905422.
[29] M. Ermis, E. Antmen, V. Hasirci, *Bioact. Mater.* **2018**, *3*, 355.
[30] S. Oh, K. S. Brammer, Y. J. Li, D. Teng, A. J. Engler, S. Chien, S. Jin, *Proc. Natl. Acad. Sci. U. S. A.* **2009**, *106*, 2130.
[31] M. J. Dalby, N. Gadegaard, R. O. Oreffo, *Nat. Mater.* **2014**, *13*, 558.
[32] S. Watari, K. Hayashi, J. A. Wood, P. Russell, P. F. Nealey, C. J. Murphy, D. C. Genetos, *Biomaterials* **2012**, *33*, 128.
[33] T. Sjöström, M. J. Dalby, A. Hart, R. Tare, R. O. Oreffo, B. Su, *Acta Biomater.* **2009**, *5*, 1433.
[34] M. J. Dalby, N. Gadegaard, R. Tare, A. Andar, M. O. Riehle, P. Herzyk, C. D. Wilkinson, R. O. Oreffo, *Nat. Mater.* **2007**, *6*, 997.
[35] J. Lovmand, J. Justesen, M. Foss, R. H. Lauridsen, M. Lovmand, C. Modin, F. Besenbacher, F. S. Pedersen, M. Duch, *Biomaterials* **2009**, *30*, 2015.
[36] L. E. McNamara, T. Sjöström, K. E. Burgess, J. J. Kim, E. Liu, S. Gordonov, P. V. Moghe, R. D. Meek, R. O. Oreffo, B. Su, *Biomaterials* **2011**, *32*, 7403.
[37] Y. Sun, C. S. Chen, J. Fu, *Annu. Rev. Biophys.* **2012**, *41*, 519.
[38] J. Hasan, H. K. Webb, V. K. Truong, S. Pogodin, V. A. Baulin, G. S. Watson, J. A. Watson, R. J. Crawford, E. P. Ivanova, *Appl. Microbiol. Biotechnol.* **2013**, *97*, 9257.
[39] K. Nowlin, A. Boseman, A. Covell, D. LaJeunesse, *J. R. Soc., Interface* **2015**, *12*, 20140999.
[40] G. S. Watson, D. W. Green, L. Schwarzkopf, X. Li, B. W. Cribb, S. Myhra, J. A. Watson, *Acta Biomater.* **2015**, *21*, 109.
[41] J. Hasan, R. J. Crawford, E. P. Ivanova, *Trends Biotechnol.* **2013**, *31*, 295.
[42] D. P. Linklater, V. A. Baulin, S. Juodkazis, R. J. Crawford, P. Stoodley, E. P. Ivanova, *Nat. Rev. Microbiol.* **2020**, *19*, 8.
[43] M. Ganjian, L. Angeloni, M. J. Mirzaali, K. Modaresifar, C. W. Hagen, M. K. Ghatkesar, P.-L. Hagedoorn, L. E. Fratila-Apachitei, A. A. Zadpoor, *Nanoscale* **2020**, *12*, 21988.
[44] M. Ganjian, K. Modaresifar, H. Zhang, P.-L. Hagedoorn, L. E. Fratila-Apachitei, A. A. Zadpoor, *Sci. Rep.* **2019**, *9*, 18815.
[45] E. P. Ivanova, J. Hasan, H. K. Webb, G. Gervinskas, S. Juodkazis, V. K. Truong, A. H. Wu, R. N. Lamb, V. A. Baulin, G. S. Watson, J. A. Watson, D. E. Mainwaring, R. J. Crawford, *Nat. Commun.* **2013**, *4*, 2838.
[46] M. Michalska, F. Gambacorta, R. Divan, I. S. Aranson, A. Sokolov, P. Noirot, P. D. Laible, *Nanoscale* **2018**, *10*, 6639.
[47] G. Hazell, P. W. May, P. Taylor, A. H. Nobbs, C. Welch, B. Su, *Biomater. Sci.* **2018**, *6*, 1424.
[48] J. Hasan, S. Jain, K. Chatterjee, *Sci. Rep.* **2017**, *7*, 41118.
[49] E. P. Ivanova, D. P. Linklater, M. Werner, V. A. Baulin, X. Xu, N. Vrancken, S. Rubanov, E. Hanssen, J. Wandiyanto, V. K. Truong, *Proc. Natl. Acad. Sci. U. S. A.* **2020**, *117*, 12598.
[50] L. D. Ghosh, J. Hasan, A. Jain, N. R. Sundaresan, K. Chatterjee, *Nanoscale* **2019**, *11*, 20766.
[51] D. P. Linklater, S. Juodkazis, R. Crawford, E. Ivanova, *Materialia* **2019**, *5*, 100197.
[52] M. Sun, G. S. Watson, Y. Zheng, J. A. Watson, A. Liang, *J. Exp. Biol.* **2009**, *212*, 3148.
[53] J. Hasan, S. Raj, L. Yadav, K. Chatterjee, *RSC Adv.* **2015**, *5*, 44953.
[54] T. L. Clainche, D. Linklater, S. Wong, P. Le, S. Juodkazis, X. L. Guével, J.-L. Coll, E. P. Ivanova, V. Martel-Frachet, *ACS Appl. Mater. Interfaces* **2020**, *12*, 48272.
[55] Y. Zhukova, C. Hiepen, P. Knaus, M. Osterland, S. Prohaska, J. W. Dunlop, P. Fratzl, E. V. Skorb, *Adv. Healthcare Mater.* **2017**, *6*, 1601244.
[56] P. S. Mathieu, E. G. Loboa, *Tissue Eng., Part B* **2012**, *18*, 436.
[57] D. Khang, J. Choi, Y.-M. Im, Y.-J. Kim, J.-H. Jang, S. S. Kang, T.-H. Nam, J. Song, J.-W. Park, *Biomaterials* **2012**, *33*, 5997.
[58] A. Ray, O. Lee, Z. Win, R. M. Edwards, P. W. Alford, D.-H. Kim, P. P. Provenzano, *Nat. Commun.* **2017**, *8*, 14923.
[59] M. D. Cabezas, B. Meckes, C. A. Mirkin, M. Mrksich, *ACS Nano* **2019**, *13*, 11144.
[60] J. Xia, Y. Yuan, H. Wu, Y. Huang, D. A. Weitz, *Biomaterials* **2020**, *248*, 120014.
[61] N. C. Gauthier, T. A. Masters, M. P. Sheetz, *Trends Cell Biol.* **2012**, *22*, 527.
[62] D. W. Dumbauld, T. T. Lee, A. Singh, J. Scrimgeour, C. A. Gersbach, E. A. Zamir, J. Fu, C. S. Chen, J. E. Curtis, S. W. Craig, *Proc. Natl. Acad. Sci. U. S. A.* **2013**, *110*, 9788.
[63] F. Martino, A. R. Perestrelo, V. Vinarský, S. Pagliari, G. Forte, *Front. Physiol.* **2018**, *9*, 824.
[64] B. Ghezzi, P. Lagonegro, N. Fukata, L. Parisi, D. Calestani, C. Galli, G. Salviati, G. M. Macaluso, F. Rossi, *Nanomaterials* **2019**, *9*, 1701.
[65] X. Wang, X. Hu, I. Dulińska-Molak, N. Kawazoe, Y. Yang, G. Chen, *Sci. Rep.* **2016**, *6*, 28708.
[66] K. Yang, K. Jung, E. Ko, J. Kim, K. I. Park, J. Kim, S.-W. Cho, *ACS Appl. Mater. Interfaces* **2013**, *5*, 10529.
[67] J. Stricker, Y. Aratyn-Schaus, P. W. Oakes, M. L. Gardel, *Biophys. J.* **2011**, *100*, 2883.
[68] S. Di Cio, J. E. Gautrot, *Acta Biomater.* **2016**, *30*, 26.
[69] Y. Song, J. Soto, B. Chen, L. Yang, S. Li, *Biomaterials* **2020**, *234*, 119743.
[70] M. Versaevel, T. Grevesse, S. Gabriele, *Nat. Commun.* **2012**, *3*, 671.
[71] I. Casanellas, A. Lagunas, Y. Vida, E. Pérez-Inestrosa, J. A. Andrades, J. Becerra, J. Samitier, *Biomimetics* **2019**, *4*, 43.
[72] S. Stewart, A. Darwood, S. Masouros, C. Higgins, A. Ramasamy, *Bone Jt. Res.* **2020**, *9*, 1.
[73] M. J. P. Biggs, M. J. Dalby, *Proc. Inst. Mech. Eng., Part H* **2010**, *224*, 1441.
[74] C. B. Khatiwala, P. D. Kim, S. R. Peyton, A. J. Putnam, *J. Bone Miner. Res.* **2009**, *24*, 886.
[75] R. M. Salasznyk, R. F. Klees, W. A. Williams, A. Boskey, G. E. Plopper, *Exp. Cell Res.* **2007**, *313*, 22.
[76] L. Yang, L. Ge, P. van Rijn, *ACS Appl. Mater. Interfaces* **2020**, *12*, 25591.
[77] M. J. Barron, C.-J. Tsai, S. W. Donahue, *J. Biomech. Eng.* **2010**, *132*, 041005.
[78] K. Jindai, K. Nakade, K. Masuda, T. Sagawa, H. Kojima, T. Shimizu, S. Shingubara, T. Ito, *RSC Adv.* **2020**, *10*, 5673.
[79] L. Rizzello, B. Sorce, S. Sabella, G. Vecchio, A. Galeone, V. Brunetti, R. Cingolani, P. P. Pompa, *ACS Nano* **2011**, *5*, 1865.
[80] A. Persat, *Curr. Opin. Microbiol.* **2017**, *36*, 1.
[81] C. Berne, C. K. Ellison, A. Ducret, Y. V. Brun, *Nat. Rev. Microbiol.* **2018**, *16*, 616.
[82] Y. F. Dufrêne, A. Persat, *Nat. Rev. Microbiol.* **2020**, *18*, 227.
[83] M. E. Berginski, S. M. Gomez, *F1000Research* **2013**, *2*, 68.
[84] U. Horzum, B. Ozdil, D. Pesen-Okvur, *MethodsX* **2014**, *1*, 56.